

# Experimental identification of topological defects in 2D colloidal glass

Vinay Vaibhav<sup>1,\*</sup>, Arabinda Bera<sup>1,\*</sup>, Amelia C. Y. Liu<sup>2</sup>, Matteo Baggioli<sup>3‡</sup>, Peter Keim<sup>4,5,6‡</sup>, and Alessio Zaccone<sup>1‡</sup>

<sup>1</sup>Department of Physics “A. Pontremoli”, University of Milan, via Celoria 16, 20133 Milan, Italy

<sup>2</sup>School of Physics and Astronomy, Monash University, Clayton, 3800, Victoria, Australia

<sup>3</sup>Wilczek Quantum Center, School of Physics and Astronomy, Shanghai Jiao Tong University, Shanghai 200240, China & Shanghai Research Center for Quantum Sciences, Shanghai 201315, China

<sup>4</sup>Institut für Experimentelle Physik von Kondensierter Materie, Heinrich-Heine-Universität Düsseldorf, 40225 Düsseldorf, Germany

<sup>5</sup>Max-Planck-Institute for Dynamics and Self-Organization, 37077 Göttingen, Germany

<sup>6</sup>Institute for the Dynamics of Complex Systems, University of Göttingen, 37077 Göttingen, Germany

\*These authors contributed equally to this work.

‡Corresponding authors: [b.matteo@sjtu.edu.cn](mailto:b.matteo@sjtu.edu.cn); [peter.keim@uni-duesseldorf.de](mailto:peter.keim@uni-duesseldorf.de); [alessio.zaccone@unimi.it](mailto:alessio.zaccone@unimi.it);

## ABSTRACT

Topological defects are singularities in the order parameter space that are mathematically described by topological invariants and cannot be removed by continuous transformations. These defects play a significant role in various fields, ranging from cosmology to solid-state physics and biological matter. The definition of these irregularities requires an ordered reference configuration, leading to decades of debate about the existence of topological defects in disordered systems, such as glasses. Recently, it has been proposed that well-defined topological defects might emerge in the dynamical properties of glasses under deformation, potentially relating to their plastic behavior. In this study, we investigate a two-dimensional colloidal glass system composed of particles interacting by an effective magnetic repulsion. We reveal the presence of topological defects in the eigenspace of the vibrational frequencies of this experimental 2D amorphous solid. The vibrational density of states of this 2D amorphous material exhibits distinct glassy properties such as the presence of a boson peak anomaly. Through extensive numerical and theoretical quantitative analysis, we establish a robust positive correlation between the vibrational characteristics and the total number of topological defects. We furthermore show that defects of opposite charge tend to pair together and prove their local statistical correlation with the “soft spots”, the regions more prone to plastic flow. This work provides the experimental confirmation for the existence of topological defects in disordered systems revealing a complex interplay between topology, disorder, and vibrational behavior.

## Introduction

Topological defects (TD) represent a ubiquitous hallmark of nature across different scales and they are generally defined as singularities in a local order parameter [1]. They can appear in a wide range of physical systems [2–4], including but not limited to liquid crystals, superconductors, superfluids, ferromagnets, biological systems [5], and also our early universe [6]. Despite being microscopic in nature, TD can exert macroscopic influences on the behavior of the entire system. For example, they have a strong influence on the optical properties of liquid crystals and play crucial roles in various biological processes, including cell division, tissue formation, and the motion of cellular aggregates [7].

In the realm of condensed matter physics [8], the emergence of these defects disrupts ordered states [9] influencing collective excitations and even triggering phase transitions, such as the Kosterlitz, Thouless, Halperin, Nelson, Young (KTHNY) transition [10–12] in two-dimensional solids, investigated in a colloidal mono-layer very similar to the given one [13]. These defects possess distinct (topological) charges and exhibit robustness against continuous structural deformations, rendering them essential for understanding the fundamental properties of materials and being totally different from other non-topological defects such as vacancies or interstitials.

Topological defects in 3D crystalline solids manifest as dislocations and disclination lines [9, 14], providing structural irregularities within the otherwise ordered lattice, and the elementary carriers of plasticity. Dislocations, in particular, allow for the motion of crystalline planes sliding over each other (glide motion). The plasticity of crystalline solids is by now fully

understood in terms of dislocation dynamics and dislocation networks, based on seminal concepts introduced by Taylor [15], Polanyi [16] and Orowan [17]. In 2D, topological defects are point defects and their thermal dissociation cause the elastic moduli to disappear [18].

In amorphous solids, instead, the absence of long-range order complicates the identification and characterization of topological defects (since, by definition, an ordered background is needed in order to detect its irregularities), posing a big challenge in linking structure with dynamics and predicting mechanical properties from the undeformed material configuration. The chase for structural topological defects in amorphous solids, borrowing from the concepts widely used for crystals, is certainly not new and dates back to the early 70's [19]. Despite various efforts [20–30], it was nevertheless concluded that topological arguments cannot be properly applied to the case of glasses and that the predictions of the dynamical and topological arguments disagree with results found in computer simulations [31].

Therefore, apart from isolated cases [32, 33], the identification of the plastic carriers and of the “soft spots”, the regions (or particle clusters) more prone to plastic flow, in glasses remained based until now on the so-called structural indicators [34] (e.g., [35–41]) and on the phenomenological concept of shear transformation zones (STZ) [42, 43]. On the other hand, structural “soft spots”, where particle rearrangements are initiated, have been postulated to be analogous to dislocations in crystalline solids [44] but lacking any formal definition and topological character.

Recent advances in simulation and theory [45] have pursued the idea of looking for topological defects in glasses using dynamical quantities such as the displacement vector field or the eigenvector field of normal mode vibrations, instead of the seemingly featureless structure. Following this idea, Baggioli et al. [46] have unveiled well-defined topological defects in polymer glasses under shear deformation. These topological defects are predicted by theory [47] as singularities in the microscopic displacement field, and are mathematically described by a continuous-valued Burgers vector (in accord with an early intuition of Klemm and Friedel [48]). In amorphous solids, the atomic displacement field under an external deformation comprises two vector fields, one of which is fully ordered and is called the affine displacement field. This is simply the trajectory along which each atom moves as a consequence of the external strain field. The other vector field is known as the nonaffine displacement field and is much more random and irregular. It arises due to the local force imbalance on each atom in its affine position, where it is subject to a non-vanishing force (due to the lack of inversion symmetry) communicated by its neighbours [49, 50]. In this sense, the affine component of the displacement field represents the ordered background disrupted by the topological defects living within (but not being equivalent to) the nonaffine displacements.

Following a similar logic, recent simulations of two-dimensional glassy model systems at  $T = 0$  by Wu et al. [51] have revealed the presence of well-defined topological defects (of different nature) within the eigenvector field of vibrational modes, defined using the concepts of winding number and vortex structure [9]. In this second scenario, the ordered reference configuration, with respect to which defects are identified, is provided by the plane-wave eigenvector field. Both methods, [46] and [51], have demonstrated a tight connection between these TD and plastic deformations, proving the capability of these structures to predict plastic spots and to correlate with the yielding transition.

Even more recently, mixing the ideas of [46] and [51], numerical investigations by Falk and collaborators [52] have identified saddle-like topological defects with quantized -1 charge in the displacement field, generating Eshelby-like quadrupolar fields which align to form the shear bands responsible for the yielding of amorphous solids [53, 54]. Interestingly, shear banding is directly related to the percolation of STZ, whose dynamics have been shown [55] to be intimately connected to vortex-like structures as those proposed by Wu et al. [51]. Finally, although topological charge neutrality is always enforced by the conservation of global elastic dipole charge, the yielding process in amorphous systems has been related to the clustering of net negative topological charge [56].

Topological defects in crystals can be also defined in terms of geometrical properties (curvature and torsion) [9]. A similar approach based on geometry has been recently proposed by Moshe, Procaccia and collaborators as the origin of plastic screening in amorphous materials [57, 58], where the defects are identified with the elastic (dipolar and quadrupolar) charges. Interesting results in this context can be also obtained in terms of a tensorial form of electromagnetism known as vector charge tensor gauge theory [59] that is able to reproduce the structure of static stress correlations in granular materials [60].

Importantly, all such characterisations of topological defects in amorphous materials have been performed using numerical simulations. Until now, no direct observation of topological defects in experimental amorphous systems has been reported. Given the importance of topological predictors of physical properties from biological tissues to cosmology, being able to detect topological defects in disordered structures experimentally is *per se* a fundamental goal of contemporary science.

Colloidal glasses have been proved to be an excellent experimental setup to test the validity of various measures and theories related to structure and dynamics [61, 62]. Using optical microscopy, one has direct access to the structural information at the particle level. In this experimental study, we use a specific type of a colloidal particles which become magnetised in the presence of a magnetic field and form a two-dimensional disordered structure. The particles interact via dipole-dipole repulsive interaction, so, based on particle positions, we can also directly infer the pairwise interaction energy. Using this information, we construct the dynamical matrix (Hessian) of the system, and perform the identification of topological defects in the field of

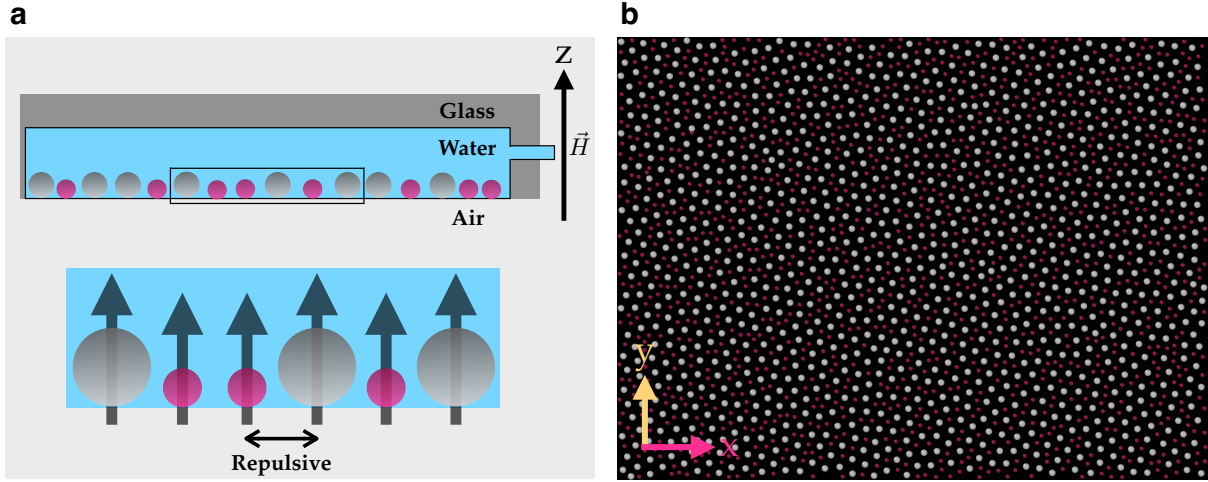


**Figure 1.** **a** A representative snapshot of the colloidal system showcasing large and small particles colored in silver and pink, respectively. **b** The arrangement of colloidal particles forming a two-dimensional monolayer, subject to a constant external magnetic field  $H$  oriented perpendicular to the surface.

normal modes. In this process, the analysis of the experimental data reveal unique features of vibrational characteristics of the system, and also the corresponding correlation with topology and “soft spots”. Our experimental study demonstrates the existence of well-defined topological defects in the vibrational field of a finite temperature 2D colloidal glass, suggesting further experimental studies that can employ these defects to understand the thermal and mechanical properties of many complex, disordered systems.

## Experimental setup

Our experimental setup comprises a colloidal monolayer, where individual particles sediment to a flat water/air interface in a hanging-droplet configuration under the influence of gravity. These colloidal particles have two different masses and diameters, forming a binary mixture (Fig.1b), and exhibit Brownian motion within the two-dimensional plane (see Methods for details). The particle interactions are paramagnetic in nature, hence a magnetic dipole moment is induced in each particle when an external magnetic field is applied perpendicular to the surface, leading to a pairwise dipole-dipole interaction potential of the form  $E_{\text{pot}} \sim 1/r^3$ , where  $r$  is the inter-particle distance. The strength of the interaction can be controlled by the external magnetic field  $H$ , setting the characteristic energy scale of the system. A crucial parameter governing the system’s behavior is represented by  $\Gamma = E_{\text{pot}}/E_{\text{kin}}$ , denoting the ratio of potential energy (stemming from this mutual dipolar interaction among particles) to the kinetic energy ( $E_{\text{kin}} \sim T$ ) arising from thermal motion. It can be interpreted as an inverse temperature or more didactically as dimensionless pressure. For our study, we set  $\Gamma = 423$ , a value at which the system is deep in a glassy state [63]. Optical microscopy is employed to record the particle positions in the field of view at a certain interval of time (Fig.1a). The experimental setup is described in detail in [64], while the structure and dynamics of this system have been studied in previous work [65, 66].

## Vibrational properties

Using the long-range dipole-dipole interaction potential among the particles, we numerically construct the dynamical (Hessian) matrix which is diagonalized to obtain the eigenvectors  $\vec{e}_l$  and eigenfrequencies  $\lambda_l$ . Here,  $\lambda_l$  indicate the  $l$ -th eigenvalue with  $l = 1, \dots, 2N$ ;  $N$  being the number of particles in the field of view. From the eigenvalues, we derive the corresponding eigenfrequencies  $\omega_l^2 = \lambda_l$  (using a mass-rescaled Hessian, see Methods). As expected from amorphous solids at finite temperature [67], the spectrum displays a fraction of negative eigenvalues, corresponding to unstable modes with purely imaginary frequency. These unstable modes correspond to dynamics over regions of the potential landscape with locally negative curvature (*e.g.*, saddle points and potential barriers) and they are widely observed in supercooled liquids as well [68]. For the unstable part of the spectrum ( $\lambda < 0$ ), we follow the practice of re-defining a positive definite frequency  $\tilde{\omega} = -i\sqrt{\lambda}$  and plotting the corresponding vDOS on the negative frequency axes upon identifying  $\tilde{\omega} = -\omega$ . The results for the experimental vibrational density of states (vDOS)  $D(\omega)$  are shown in Fig. 2a.

As highlighted in the inset of Fig. 2a, the low frequency behavior of the vDOS shows a linear scaling,  $D(\omega) \sim \omega$ . This behavior is compatible with Debye’s law in two spatial dimensions but it is also a characteristic feature of the vDOS of systems

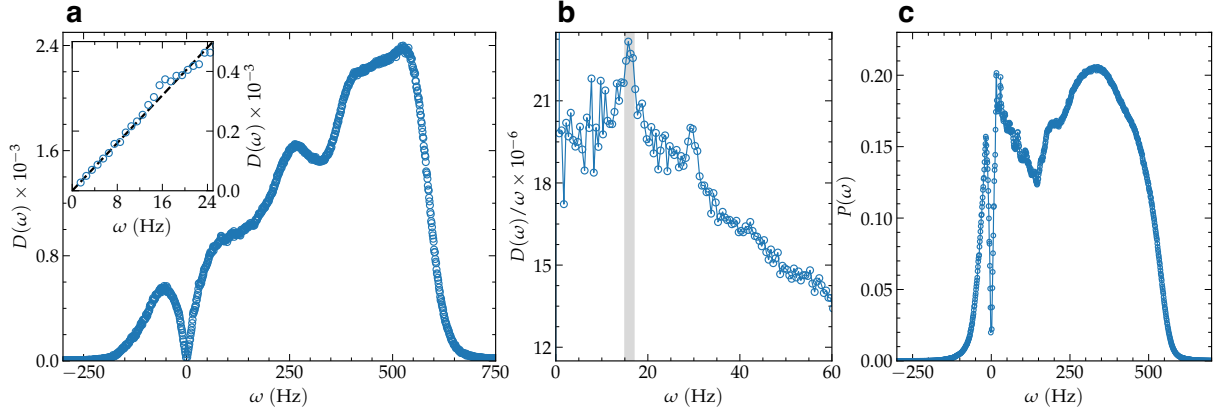


**Figure 2.** **a** The vibrational density of states  $D(\omega)$  is presented, with the inset highlighting the low-frequency behavior. The dashed line represents a linear trend, consistent with Debye’s prediction  $D(\omega) \sim \omega^{d-1}$ , where  $d = 2$ . **b**  $D(\omega)/\omega$  versus  $\omega$  is plotted at low frequencies, with shaded regions indicating the occurrence of the boson peak. **c** The participation ratio  $P(\omega)$  versus  $\omega$  is depicted, providing insights into the localization properties of vibrational modes across different frequency ranges.

with unstable modes [69, 70]. Interestingly, we observe that the vDOS is symmetric at low frequency and the linear scaling (including the corresponding slope) is the same for the stable and unstable branches. We also notice that only the stable branch can be directly interpreted as pertaining to vibrational modes *stricto sensu*.

In Fig. 2b, we present the same vDOS normalized by the low-frequency linear (Debye) scaling,  $D(\omega)/\omega$ . In this representation, the presence of an anomalous peak is clear around a characteristic frequency  $\omega_{BP}$ , marked within error bars by the shaded vertical strip (15 – 17 Hz). This vibrational anomaly over Debye’s law is known as “boson peak” and it is a common feature of amorphous materials [71]. Despite the huge effort devoted to characterize and comprehend this feature in 3D systems, its experimental detection in quasi two-dimensional (2D) amorphous materials remains limited [72–74]. In this respect, our result provides another experimental identification of the BP anomaly in a specific type of 2D amorphous materials – colloidal glasses – using directly the Hessian matrix rather than the covariance matrix.

To measure the extent of mode localization, we also calculate the participation ratio  $P(\omega)$ , plotted in Fig. 2c. We observe a sharp peak corresponding to acoustic phonon-type excitations at very low (positive) frequency, and a secondary broader peak at higher frequency possibly linked to optical-like excitations due to the particle size mismatch. This secondary peak then drops sharply in correspondence of the Anderson-localized highest frequency modes which terminate at the Debye frequency of the system. The participation ratio for the unstable branch features the typical behavior observed many times in the past for glassy materials [75, 76].

## Topological defects

We move to the analysis of the spatial structure of the vibrational modes by investigating the corresponding eigenvector fields. In order to identify and characterize the topological properties of the eigenvector field, we resort to the method originally proposed by Wu et al. [51], based on the computation of the local winding number  $q$ . By considering the smallest square grid in our experimental data, we identify vortices (anti-vortices) as topological defects with winding number (or equivalently topological charge)  $q = +1$  ( $-1$ ).

Figures 3a-d provide visual representations of the eigenvector fields at various frequencies, with filled red and blue circles denoting the locations of vortices and anti-vortices, respectively. Additionally, the color map indicates the local angle of the eigenvector field with respect to the  $x$ -axes. The structure of the eigenvector field is evidently highly heterogeneous, displaying several vortex-like structures and singularities. Notably, the eigenvectors at lower frequencies exhibit a smaller number of topological defects. This suggests that the number of defects grows with frequency and becomes more uniformly distributed in space. Significantly, at lower frequencies, there are fewer topological defects, and a rich, co-operative and swirling eigenfield structure. This might be related to the fact that at low-frequency the dynamics are dominated by plane waves, displaying a periodic structure of swirling (see *e.g.* Fig.3 in [77]). Conversely, at higher frequencies, there is a notable increase in defect density, with defects uniformly distributed throughout the space and reduced coherence in the eigenvector field. Interestingly, topological defects can be also found in the eigenvectors corresponding to unstable modes, *e.g.* panel a in Fig. 3.

Figure 4a presents the vibrational density of states  $D(\omega)$  and the total number of defects  $N_d$  against vibrational frequencies within the same frame. This highlights a robust correlation between these quantities across the entire frequency spectrum.

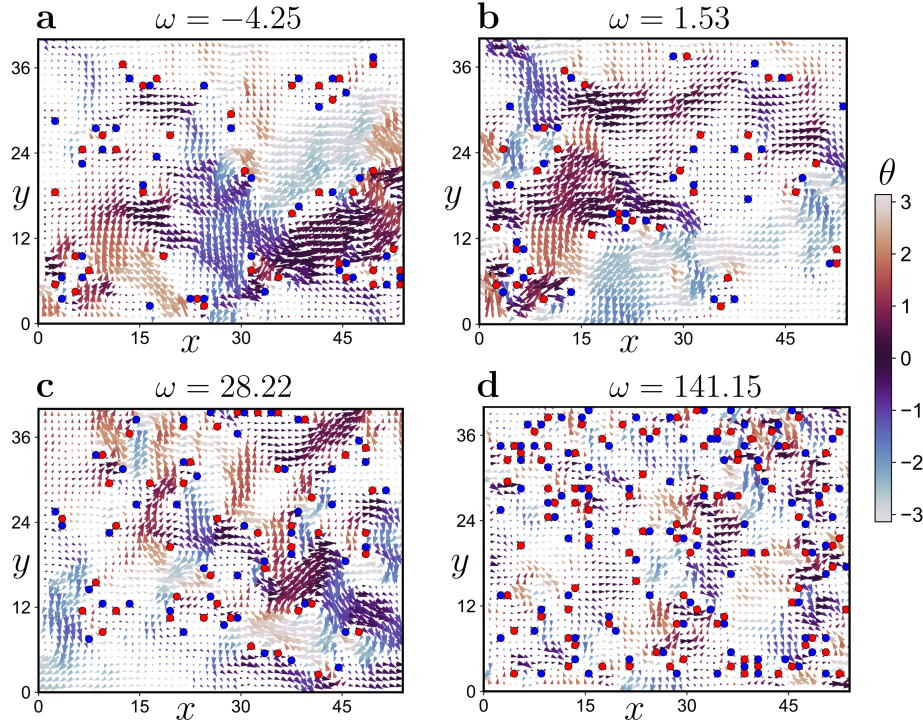


**Figure 3.** **a-d** Eigenvector fields within a rectangular field of view ( $54a \times 40a$ , where  $a = 20.78 \mu\text{m}$ ) are depicted for various eigenfrequencies ( $\omega = -4.25, 1.53, 28.22$ , and  $141.15$ ). The color bar denotes the phase of the eigenvectors ( $\theta = \tan^{-1}(e_y/e_x)$ ), capturing the directional information of the vibrational modes. The size of the arrow head indicates the magnitude of the eigenvector field at that point. Topological defects are indicated by filled circles, with red and blue representing  $q = +1$  and  $-1$  respectively, highlighting the presence of non-trivial topological features within the two-dimensional colloidal glass system.

The inset of Fig. 4a delves into the low-frequency behavior of  $N_d$ , where dashed line signifies the linear dependence on  $\omega$ . This linear dependence is different from what observed in a zero temperature simulation glass model in [51], where  $N_d$  scales quadratically with the frequency at low energy. In the Supplementary Information, using simulations, we prove that this difference is due to the finite temperature dissipative effects and we recover the results of [51] in the zero temperature limit.

To further establish the correlation between vibrational properties and topological defects, we calculate the Pearson correlation coefficient,  $C(\omega)$ , at various  $\omega$  values, considering data points within a specified frequency range  $\omega - \Delta\omega/2$  to  $\omega + \Delta\omega/2$ . Figure 4b illustrates the variation of  $C(\omega)$  for different frequency width values ( $\Delta\omega = 50, 75$ , and  $100$ ). We observe that the fluctuations of  $C(\omega)$  decrease as the frequency width increases. The proximity of  $C$  values to unity across the majority of the spectrum signifies a robust correlation between  $D(\omega)$  and  $N_d$ . However, intriguingly, instances of strong anti-correlation are observed within specific frequency ranges, as highlighted by gray vertical stripes in Fig. 4a and Fig. 4b. Particularly noteworthy is the presence of such anti-correlation within the frequency range  $\omega \in [250, 340]$ , prompting further theoretical investigation to unravel its origin and its consequential impact on the system's structure and dynamics.

### Structural features of defects and their correlation with soft spots

To understand the spatial organization of defects, we calculate partial pair correlation functions  $g_{PP}(r)$ ,  $g_{PN}(r)$  and  $g_{NN}(r)$  for positive-positive, positive-negative and negative-negative defect pairs respectively, as shown in Fig. 5. From the positive-positive and negative-negative defect correlation in Fig. 5a and c, it is clear that, for small  $r$ , there is no correlation (or even a “depletion” zone near contact), indicating the absence of defects with similar charge in the vicinity of a tagged defect. Instead, the positive-negative correlation in Fig. 5b shows a very high probability for the presence of another defect with opposite charge in the neighborhood of a tagged defect. This observation suggests that defect charges with the same sign repel each other and those with opposite sign attract each other. It appears that the repulsion between two defects both with negative sign is slightly stronger because the repulsive “hard-core” distance at small separation  $r$  in  $g_{NN}$  is bigger than that in  $g_{PP}$ . Overall, both attraction and repulsion become weaker with the increase in frequency  $\omega$ , and at sufficiently high  $\omega$  such defects are expected

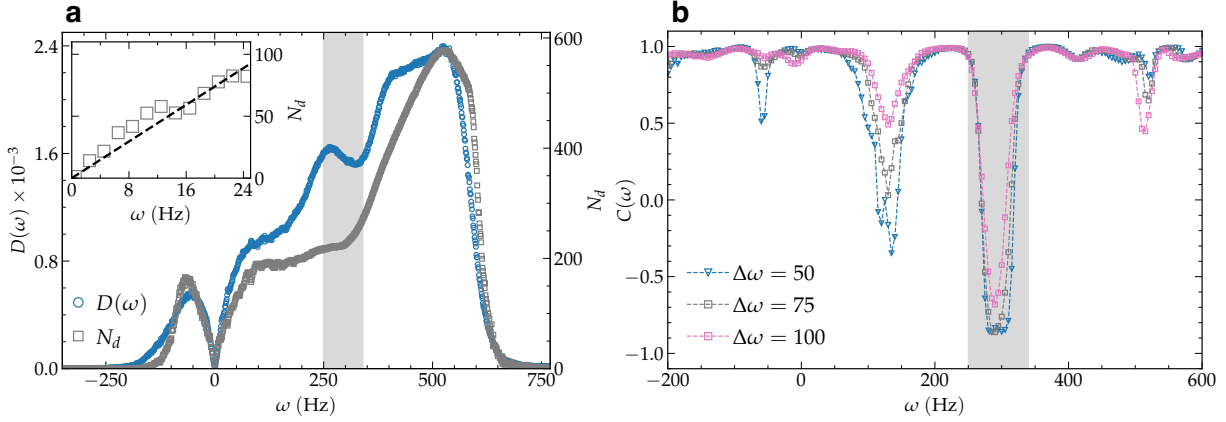


**Figure 4.** **a** The vibrational density of states ( $D(\omega)$ ) and the total number of defects ( $N_d$ ) are plotted against vibrational frequencies. The left-side vertical axis corresponds to  $D(\omega)$ , while the right-side axis corresponds to  $N_d$ . The inset illustrates the low-frequency behavior, with solid lines indicating linear trends. **b** Pearson correlation coefficients ( $C$ ) between  $D(\omega)$  and  $N_d(\omega)$  are depicted for varying  $\omega$ , considering three different frequency widths:  $\Delta\omega = 50, 75$ , and  $100$ . The shaded gray area marks the frequency range  $\omega \in [250, 340]$ , where strong anti-correlation is observed in both panels **a** and **b**.

to be completely uncorrelated and homogeneously distributed.

In recent studies, it has been possible to identify “soft spots” in the low-frequency vibrational modes where mesoscale relaxation or rearrangements are prone to happen [44, 78]. We identify such soft spots in the present system using the softness field defined in [78] (see Methods for details) and calculate their radial pair correlation with positive ( $g_{PS}(r)$ ) and negative ( $g_{NS}(r)$ ) defects (see Methods and SI). Figures 5d-e show the correlation for  $\omega = 15, 20, 30, 50, 100$ . It is quite evident that the defects with negative charge are highly correlated with soft spots at small  $r$ , while defects with positive charge show no such correlation. This means negative charge defects tend to appear in the close vicinity of soft spots. Furthermore, it will be expected that these defects with negative charge will most likely be associated with mobile regions in structural relaxation or plastic rearrangements under deformation. Defects with positive charge located somewhat further away from the soft spots are also correlated, evidenced by the peak in  $g_{PS}$  at  $r \approx 40 \mu\text{m}$ . This is expected because we have already seen a significant correlation between +1 and -1 defects at the same length-scale, see Fig. 5b. With the increase in  $\omega$ , the correlation becomes weaker with both types of defects.

## Discussion and conclusions

Based on our experimental findings and analysis, we have successfully explored the topological characteristics of a two-dimensional colloidal glass system under the influence of an external magnetic field. Through meticulous control of experimental parameters and advanced numerical techniques, we have revealed intriguing insights into the interplay between topology, vibrational properties, and defect dynamics within disordered systems.

Our investigation has unveiled the presence of topological defects within the eigenspace of vibrational frequencies of an experimental 2D colloidal glass. This provides a direct experimental observation of topologically non-trivial features in a colloidal glass. Notably, the observed correlation between the vibrational density of states (vDOS) and the total number of defects underscores the profound influence of topology on the material’s vibrational behavior. The robustness of this correlation, as evidenced by the Pearson correlation coefficient analysis, highlights the significance of topological defects in shaping the structural and dynamical properties of colloidal glasses.

By analyzing the structural properties of the topological defects, we have shown that defects of opposite charge pair together while defects with same charge repel each other, as expected from our intuition from electromagnetism. More importantly, we have observed a strong correlation at short distance between defects with negative topological charge and soft spots, confirming a close relation between anti-vortices and plasticity as suggested in [51]. Interestingly, we have found that a correlation between positive defects and plastic spots exist at larger length-scales as well, and it is possibly due to the positive correlation between negative and positive defects appearing at the same scale.

Our experimental analysis complements and confirms several of the results previously obtained from simulations at zero temperature [51], but it also provides several important new lessons and clarifications. First, it proves that the topological vortex-like defects proposed in [51] survive at finite temperature. Second, it clarifies that the number of these defects in realistic, and necessarily finite temperature, systems does not scale quadratically with frequency, as argued in [51], but rather linearly

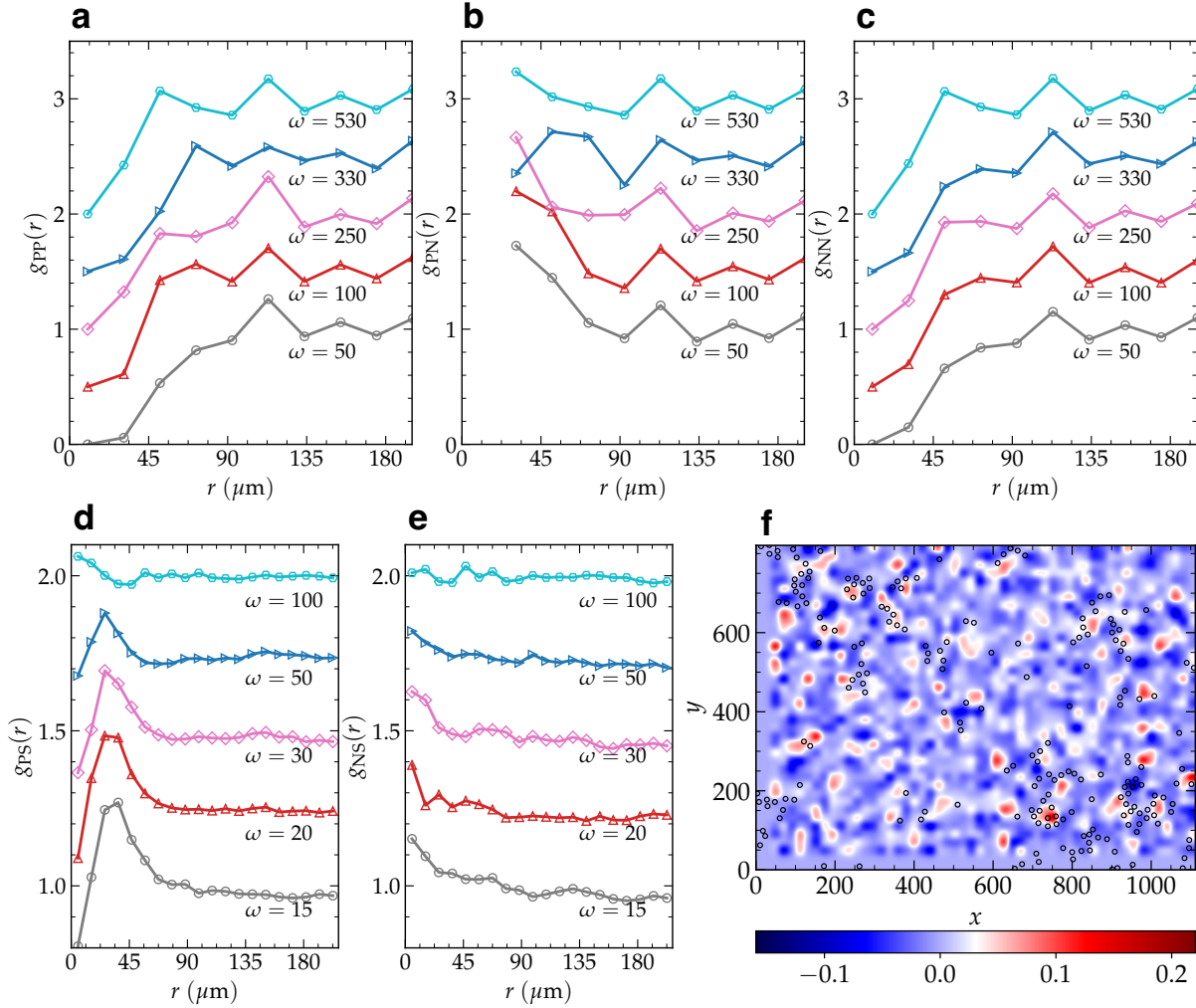


**Figure 5.** **a-c** Pair correlation functions for positive-positive, positive-negative and negative-negative defect pairs ( $g_{PP}(r)$ ,  $g_{PN}(r)$  and  $g_{NN}(r)$ ), respectively, for different  $\omega$  values. Plots other than  $\omega = 50$  are shifted by the multiple of 0.5 for clarity. **d-e** Spatial correlation between soft spots (with top 10% softness) and topological defects with **d** positive charge  $g_{PS}(r)$ , and **e** negative charge  $g_{NS}(r)$ , for different  $\omega$  values. For better clarity, curves other than  $\omega = 15$  are shifted upward by the multiple of 0.25. **f** Color map of charge density field obtained by the  $\omega^{-1}$  weighted averaging of topological charge over frequencies in the range  $0 < \omega < 50$ , shown together with the soft spots (open symbols).

with it, nicely correlating with the vibrational properties of the system. Finally, our experimental data supports the claim of [51] of a strong local correlation between the -1 defects and plastic spots at short scales. Nevertheless, they also reveal a strong correlation with the +1 defects at an intermediate larger scale, that is consistent, and indeed expected, from the strong correlation among +1 and -1 defects. This suggests that +1 and -1 defects tend to pair together and create dipole structures, with possible intriguing connections with recent results about plastic screening in amorphous systems by Lemaître et al. [57].

In conclusion, our study on a sedimented 2D colloidal glass with ideal dipole-dipole interactions demonstrates the existence of mathematically well-defined topological defects in a completely disordered experimental system. This finding suggests that similar analytical approaches may be usefully extended to other structural glasses. It contributes to advancing our understanding of the intricate interplay between topology, vibrational properties, and defect dynamics in disordered systems. The insights gained from this research not only deepen our knowledge of disordered materials, but also pave the way for future explorations aimed at uncovering the fundamental principles governing the mechanical and thermal behavior of complex materials. As our understanding continues to evolve, we anticipate that further studies will shed light on new phenomena related to the present observations, and unveil novel avenues for exploration in condensed matter physics, biology, materials science and cosmology.

## Methods

### Experimental details

We consider here an experimental setup of an equimolar binary colloidal mixture (consisting of species A and B) of spherical particles in 2D, with two different magnetic moments. The two species have diameters  $d_A = 4.5 \mu\text{m}$ ,  $d_B = 2.8 \mu\text{m}$ , magnetic susceptibilities (per particle)  $\chi_A = 6.2 \times 10^{-11} \text{ Am}^2/\text{T}$ ,  $\chi_B = 6.6 \times 10^{-12} \text{ Am}^2/\text{T}$  and mass densities  $\rho_A = 1.5 \text{ g/cm}^3$ ,  $\rho_B = 1.3 \text{ g/cm}^3$ . A constant magnetic field  $H = 3.9 \times 10^{-3} \text{ T}$  is applied perpendicular to the plane containing the particles which induces magnetic moment  $M_A = \chi_A H$  or  $M_B = \chi_B H$  in each particle, thus, particles interact via the dipole-dipole pair potential with each other. The potential energy between two constituent particles separated by a distance  $r$  is given by

$$V_{\alpha\beta}(r) = \frac{\mu_0}{4\pi} \frac{M_\alpha M_\beta}{r^3}, \quad (1)$$

with  $\alpha, \beta \in \{A, B\}$  and  $\mu_0 = 4\pi \times 10^{-7} \text{ Tm/A}$  is the vacuum permeability. Here we have approximately  $N = 2300$  number of particles in the rectangular field of view  $1158 \times 865 \mu\text{m}^2$  in each sample.

### Vibrational analysis

We obtain eigenvalues  $\lambda_l$  ( $l = 1, 2, \dots, 2N$ ) and associated eigenmodes by diagonalizing the dynamical (Hessian) matrix given by

$$H_{ij} = \frac{1}{\sqrt{m_i m_j}} \frac{\partial^2 U}{\partial r_i \partial r_j}. \quad (2)$$

Here  $m_i$  and  $r_i$  are the mass and spatial coordinates of the  $i$ th colloidal particle respectively. Also,  $U = \sum_{\alpha < \beta} V_{\alpha\beta}$  is the potential energy of the system. Further, we estimate the eigenfrequencies as  $\omega_l = \sqrt{\lambda_l}$ . From the distribution of  $\omega$ , we obtain the vibrational density of states (vDOS)

$$D(\omega) = \frac{1}{2N-2} \sum_l \delta(\omega - \omega_l). \quad (3)$$

Note that, we conventionally represent the imaginary frequencies with negative values while showing the density of states.

### Characterization of topological defects

For each eigenvector field  $(e_i^x, e_i^y)$  at  $\omega_i$  ( $i = 1, 2, \dots, 2N$ ), we assign an angle  $\theta(\vec{r})$  on every site at  $\vec{r}$  of a  $54 \times 40$  rectangular lattice having grid length  $r_c$  in both the directions and superposed to the experimental system. We obtain the phase angle  $\theta(\vec{r})$  at each lattice site as

$$\tan \theta(\vec{r}) = \frac{\sum_i w(\vec{r} - \vec{r}_i) e_i^y}{\sum_i w(\vec{r} - \vec{r}_i) e_i^x}, \quad (4)$$

where  $\vec{r}_i$  is the location of particle  $i$ , and  $w(\vec{r} - \vec{r}_i)$  is a Gaussian weight function, defined to be  $w(\vec{r} - \vec{r}_i) = \exp(-|\vec{r} - \vec{r}_i|^2 / r_c^2)$  with  $r_c = 20.78 \mu\text{m}$  (lattice spacing).

We determine the topological charge  $q$  inside each smallest square grid by evaluating the line integral of  $\vec{\nabla} \theta$  over a closed path inside the lattice, given by

$$q = \frac{1}{2\pi} \oint \vec{\nabla} \theta \cdot \vec{d}\ell, \quad (5)$$

where  $\vec{d}\ell$  represents the line element along the closed square loop. Typically, the value of  $q$  is an integer, and it is used to identify the locations of defects, which are characterized by non-zero values of  $q$  at the center of the smallest square regions. For the calculation of topological charge, we do not enforce the periodic boundary conditions. We calculate the total number of defects  $N_d$  by counting the defects with  $q = +1$  and  $-1$ .

### Calculation of correlation coefficients

The Pearson correlation coefficient  $C(\omega)$  is calculated as

$$C(\omega) = \frac{\sum_{\{\omega\}} (D(\omega) - \bar{D}(\omega))(N_d(\omega) - \bar{N}_d(\omega))}{\sqrt{\sum_{\{\omega\}} (D(\omega) - \bar{D}(\omega))^2} \sqrt{\sum_{\{\omega\}} (N_d(\omega) - \bar{N}_d(\omega))^2}}, \quad (6)$$



where  $\bar{D}(\omega)$  and  $\bar{N}_d(\omega)$  are the average value of  $D(\omega)$  and  $N_d(\omega)$ , respectively, within the considered range of  $\omega \in [\omega - \Delta\omega/2, \omega + \Delta\omega/2]$ , where  $\Delta\omega$  defines the frequency width.

To ensure a thorough examination of the correlation between  $D(\omega)$  and  $N_d(\omega)$  across the frequency spectrum, we employ the following approach. Initially, we compute the average data for  $D(\omega)$  and  $N_d$  across the entire range of  $\omega$ . Subsequently, we construct an interpolation function, enabling us to access the values of  $D(\omega)$  and  $N_d$  for any given  $\omega$ .

For each  $\omega$ , we interpolate  $2 \times 10^4$  data points with increasing  $\omega$  within the range  $\omega \in [\omega - \Delta\omega/2, \omega + \Delta\omega/2]$ . Utilizing this interpolated data, we then calculate  $C(\omega)$  using Eq. 6. This meticulous procedure guarantees a comprehensive assessment of the correlation between  $D(\omega)$  and  $N_d(\omega)$ , ensuring robust and reliable results across the entire frequency spectrum.

### Definition of soft spots and their correlation with topological defects

We calculate the softness field  $\phi_i$  defined for each particle  $i$  by superposing the participation fraction weighted by the corresponding mode energy in the low-frequency vibrational modes,

$$\phi_i = \frac{1}{N_m} \sum_{j=1}^{N_m} \frac{|e_j^{(i)}|^2}{m_i \omega_j^2}. \quad (7)$$

Here  $e_j^{(i)}$  is the components corresponding to particle  $i$  of the eigenvector associated with frequency  $\omega_j$  and  $N_m$  is the number of low energy modes considered for calculation. In this study,  $N_m$  is considered such that  $0 < \omega < 50$ . Further, we identify the particles with top 10% softness value as soft spots. The radial pair correlation function between the soft spots and the topological defects with positive charge in mode  $l$  is defined as

$$g_{\text{PS}}^l(r) = \frac{L_x L_y}{2\pi r N_d^l N_S} \sum_{i=1}^{N_d^l} \sum_{j=1}^{N_S} \delta(r - |\vec{r}_{ij}|), \quad (8)$$

where  $L_x, L_y$  are the dimensions of the region in which correlation is calculated,  $N_d^l$  is the number of defects with positive charge in mode  $l$  inside the region,  $N_S$  is the number of soft spots inside the region and  $|\vec{r}_{ij}|$  is the distance between topological defect  $i$  and soft spot  $j$ . Similarly,  $g_{\text{NS}}^l$ , correlation between defects with negative charge corresponding to  $\omega_l$  and soft spot can be defined.

### Data availability

The datasets generated and analysed during the current study are available upon reasonable request by contacting the corresponding authors.

### Code availability

The code that support the findings of this study is available upon reasonable request by contacting the corresponding authors.

### Acknowledgements

We would like to thank Yuliang Jin, Deng Pan, Piotr Surowka, Jie Zhang, Cunyuan Jiang, Yujie Wang, Zihan Zheng, Jack Douglas, Tim W. Sirk and Chengran Du for many discussions on topological defects in glasses and related collaborations. M.B. acknowledges the support of the Shanghai Municipal Science and Technology Major Project (Grant No.2019SHZDZX01) and the sponsorship from the Yangyang Development Fund. A.C.Y.L. acknowledges the support of the Australian Research Council (FT180100594). A.Z. and V.V. gratefully acknowledge funding from the European Union through Horizon Europe ERC Grant number: 101043968 ‘‘Multimech’’. A.Z. gratefully acknowledges the Niedersächsische Akademie der Wissenschaften zu Göttingen in the frame of the Gauss Professorship program. A.Z. and A.B. gratefully acknowledge funding from US Army Research Office through contract nr. W911NF-22-2-0256.

### Author contributions

P. K. provided the dataset of the experiment. V. V and A. B. performed the numerical analysis. A. Z. and M. B supervised the project. All authors contributed to the writing of the manuscript.

### Competing interests

The authors declare that no competing interests exist.

## References

1. Fumeron, S. & Berche, B. Introduction to topological defects: from liquid crystals to particle physics. *The Eur. Phys. J. Special Top.* **232**, 1813–1833 (2023).
2. Shankar, S., Souslov, A., Bowick, M. J., Marchetti, M. C. & Vitelli, V. Topological active matter. *Nat. Rev. Phys.* **4**, 380–398 (2022).
3. Wang, X., Miller, D. S., Bukusoglu, E., De Pablo, J. J. & Abbott, N. L. Topological defects in liquid crystals as templates for molecular self-assembly. *Nat. materials* **15**, 106–112 (2016).
4. Giomi, L., Kos, Ž., Ravnik, M. & Sengupta, A. Cross-talk between topological defects in different fields revealed by nematic microfluidics. *Proc. Natl. Acad. Sci.* **114**, E5771–E5777 (2017).
5. Ardaševa, A. & Doostmohammadi, A. Topological defects in biological matter. *Nat. Rev. Phys.* **4**, 354–356 (2022).
6. Durrer, R. Topological defects in cosmology. *New astronomy reviews* **43**, 111–156 (1999).
7. Drozdowski, O. M. & Schwarz, U. S. Morphological instability at topological defects in a three-dimensional vertex model for spherical epithelia (2024). [2403.08954](https://doi.org/10.26434/chemrxiv-2024-2403).
8. Nelson, D. R. *Defects and geometry in condensed matter physics* (Cambridge University Press, 2002).
9. Kleinert, H. *Gauge Fields in Condensed Matter* (WORLD SCIENTIFIC, 1989).
10. Kosterlitz, J. M. & Thouless, D. J. Ordering, metastability and phase transitions in two-dimensional systems. *J. Phys. C: Solid State Phys.* **6**, 1181, DOI: [10.1088/0022-3719/6/7/010](https://doi.org/10.1088/0022-3719/6/7/010) (1973).
11. Halperin, B. I. & Nelson, D. R. Theory of two-dimensional melting. *Phys. Rev. Lett.* **41**, 121–124, DOI: [10.1103/PhysRevLett.41.121](https://doi.org/10.1103/PhysRevLett.41.121) (1978).
12. Young, A. P. Melting and the vector coulomb gas in two dimensions. *Phys. Rev. B* **19**, 1855–1866, DOI: [DOI10.1103/PhysRevB.19.1855](https://doi.org/10.1103/PhysRevB.19.1855) (1979).
13. Gasser, U., Eisenmann, C., Maret, G. & Keim, P. Melting of crystals in two dimensions. *ChemPhysChem* **11**, 963–970, DOI: <https://doi.org/10.1002/cphc.200900755> (2010).
14. Landau, L. & Lifshitz, E. *Theory of Elasticity: Volume 6* (Pergamon Press, 1986).
15. Taylor, G. I. The mechanism of plastic deformation of crystals. part i. theoretical. *Proc. Royal Soc. London. Ser. A, Containing Pap. a Math. Phys. Character* **145**, 362–387 (1934).
16. Polanyi, M. Über eine art gitterstörung, die einen kristall plastisch machen könnte. *Zeitschrift für Physik* **89**, 660–664, DOI: [10.1007/BF01341481](https://doi.org/10.1007/BF01341481) (1934).
17. Orowan, E. Zur kristallplastizität. i. *Zeitschrift für Physik* **89**, 605–613, DOI: [10.1007/BF01341478](https://doi.org/10.1007/BF01341478) (1934).
18. Zippelius, A., Halperin, B. I. & Nelson, D. R. Dynamics of two-dimensional melting. *Phys. Rev. B* **22**, 2514–2541, DOI: [10.1103/PhysRevB.22.2514](https://doi.org/10.1103/PhysRevB.22.2514) (1980).
19. Gilman, J. J. Flow via dislocations in ideal glasses. *J. Appl. Phys.* **44**, 675–679, DOI: [10.1063/1.1662243](https://doi.org/10.1063/1.1662243) (1973).
20. Spaepen, F. Structural imperfections in amorphous metals. *J. Non-Crystalline Solids* **31**, 207–221, DOI: [https://doi.org/10.1016/0022-3093\(78\)90105-9](https://doi.org/10.1016/0022-3093(78)90105-9) (1978). Proceedings of the Topical Conference on Atomic Scale Structure of Amorphous Solids.
21. Cotterill, R. M. J. Dislocationlike structures in a simulated liquid. *Phys. Rev. Lett.* **42**, 1541–1544, DOI: [10.1103/PhysRevLett.42.1541](https://doi.org/10.1103/PhysRevLett.42.1541) (1979).
22. Blackett, N. R. Disclination lines in glasses. *Philos. Mag. A* **40**, 859–868, DOI: [10.1080/01418617908234879](https://doi.org/10.1080/01418617908234879) (1979).
23. Morris, R. C. Disclination-dislocation model of metallic glass structures. *J. Appl. Phys.* **50**, 3250–3257, DOI: [10.1063/1.326364](https://doi.org/10.1063/1.326364) (1979).
24. Popescu, M. Defect formation in amorphous structures as revealed by computer simulation. *Thin Solid Films* **121**, 317–347, DOI: [https://doi.org/10.1016/0040-6090\(84\)90059-2](https://doi.org/10.1016/0040-6090(84)90059-2) (1984).
25. Egami, T. & Vitek, V. Local structural fluctuations and defects in metallic glasses. *J. Non-Crystalline Solids* **61-62**, 499–510, DOI: [https://doi.org/10.1016/0022-3093\(84\)90596-9](https://doi.org/10.1016/0022-3093(84)90596-9) (1984). Proceedings of the Fifth International Conference on Liquid and Amorphous Metals.
26. Shi, L. Introduction and propagation of screw-dislocation-like defects in an amorphous lennard-jones solid. *Mater. Chem. Phys.* **36**, 68–76, DOI: [https://doi.org/10.1016/0254-0584\(93\)90009-B](https://doi.org/10.1016/0254-0584(93)90009-B) (1993).

27. Chaudhari, P., Levi, A. & Steinhardt, P. Edge and screw dislocations in an amorphous solid. *Phys. Rev. Lett.* **43**, 1517–1520, DOI: [10.1103/PhysRevLett.43.1517](https://doi.org/10.1103/PhysRevLett.43.1517) (1979).
28. T. Egami, K. M. & Vitek, V. Structural defects in amorphous solids a computer simulation study. *Philos. Mag. A* **41**, 883–901, DOI: [10.1080/01418618008243894](https://doi.org/10.1080/01418618008243894) (1980).
29. Acharya, A. & Widom, M. A microscopic continuum model for defect dynamics in metallic glasses. *J. Mech. Phys. Solids* **104**, 1–11, DOI: <https://doi.org/10.1016/j.jmps.2017.03.014> (2017).
30. Nelson, D. R. Order, frustration, and defects in liquids and glasses. *Phys. Rev. B* **28**, 5515–5535, DOI: [10.1103/PhysRevB.28.5515](https://doi.org/10.1103/PhysRevB.28.5515) (1983).
31. Steinhardt, P. J. & Chaudhari, P. Point and line defects in glasses. *Philos. Mag. A* **44**, 1375–1381, DOI: [10.1080/01418618108235816](https://doi.org/10.1080/01418618108235816) (1981).
32. Cao, Y. et al. Structural and topological nature of plasticity in sheared granular materials. *Nat. Commun.* **9**, 2911, DOI: [10.1038/s41467-018-05329-8](https://doi.org/10.1038/s41467-018-05329-8) (2018).
33. Moshe, M., Levin, I., Aharoni, H., Kupferman, R. & Sharon, E. Geometry and mechanics of two-dimensional defects in amorphous materials. *Proc. Natl. Acad. Sci.* **112**, 10873–10878, DOI: [10.1073/pnas.1506531112](https://doi.org/10.1073/pnas.1506531112) (2015). <https://www.pnas.org/doi/pdf/10.1073/pnas.1506531112>.
34. Richard, D. et al. Predicting plasticity in disordered solids from structural indicators. *Phys. Rev. Mater.* **4**, 113609, DOI: [10.1103/PhysRevMaterials.4.113609](https://doi.org/10.1103/PhysRevMaterials.4.113609) (2020).
35. Peng, H. L., Li, M. Z. & Wang, W. H. Structural signature of plastic deformation in metallic glasses. *Phys. Rev. Lett.* **106**, 135503, DOI: [10.1103/PhysRevLett.106.135503](https://doi.org/10.1103/PhysRevLett.106.135503) (2011).
36. Patinet, S., Vandembroucq, D. & Falk, M. L. Connecting local yield stresses with plastic activity in amorphous solids. *Phys. Rev. Lett.* **117**, 045501, DOI: [10.1103/PhysRevLett.117.045501](https://doi.org/10.1103/PhysRevLett.117.045501) (2016).
37. Yang, X., Liu, R., Yang, M., Wang, W.-H. & Chen, K. Structures of local rearrangements in soft colloidal glasses. *Phys. Rev. Lett.* **116**, 238003, DOI: [10.1103/PhysRevLett.116.238003](https://doi.org/10.1103/PhysRevLett.116.238003) (2016).
38. Chen, K. et al. Measurement of correlations between low-frequency vibrational modes and particle rearrangements in quasi-two-dimensional colloidal glasses. *Phys. Rev. Lett.* **107**, 108301, DOI: [10.1103/PhysRevLett.107.108301](https://doi.org/10.1103/PhysRevLett.107.108301) (2011).
39. Kapteijns, G., Richard, D. & Lerner, E. Nonlinear quasilocalized excitations in glasses: True representatives of soft spots. *Phys. Rev. E* **101**, 032130, DOI: [10.1103/PhysRevE.101.032130](https://doi.org/10.1103/PhysRevE.101.032130) (2020).
40. Mitra, S., Marín-Aguilar, S., Sastry, S., Smallenburg, F. & Foffi, G. Correlation between plastic rearrangements and local structure in a cyclically driven glass. *The J. Chem. Phys.* **156**, 074503, DOI: [10.1063/5.0077851](https://doi.org/10.1063/5.0077851) (2022).
41. Ding, J., Patinet, S., Falk, M. L., Cheng, Y. & Ma, E. Soft spots and their structural signature in a metallic glass. *Proc. Natl. Acad. Sci.* **111**, 14052–14056, DOI: [10.1073/pnas.1412095111](https://doi.org/10.1073/pnas.1412095111) (2014).
42. Falk, M. L. & Langer, J. S. Dynamics of viscoplastic deformation in amorphous solids. *Phys. Rev. E* **57**, 7192–7205, DOI: [10.1103/PhysRevE.57.7192](https://doi.org/10.1103/PhysRevE.57.7192) (1998).
43. Richard, D., Kapteijns, G., Giannini, J. A., Manning, M. L. & Lerner, E. Simple and broadly applicable definition of shear transformation zones. *Phys. Rev. Lett.* **126**, 015501, DOI: [10.1103/PhysRevLett.126.015501](https://doi.org/10.1103/PhysRevLett.126.015501) (2021).
44. Manning, M. L. & Liu, A. J. Vibrational modes identify soft spots in a sheared disordered packing. *Phys. Rev. Lett.* **107**, 108302, DOI: [10.1103/PhysRevLett.107.108302](https://doi.org/10.1103/PhysRevLett.107.108302) (2011).
45. Baggioli, M. Topological defects reveal the plasticity of glasses. *Nat. Commun.* **14**, 2956, DOI: [10.1038/s41467-023-38549-8](https://doi.org/10.1038/s41467-023-38549-8) (2023).
46. Baggioli, M., Kriuchevskiy, I., Sirk, T. W. & Zaccane, A. Plasticity in amorphous solids is mediated by topological defects in the displacement field. *Phys. Rev. Lett.* **127**, 015501, DOI: [10.1103/PhysRevLett.127.015501](https://doi.org/10.1103/PhysRevLett.127.015501) (2021).
47. Baggioli, M., Landry, M. & Zaccane, A. Deformations, relaxation, and broken symmetries in liquids, solids, and glasses: A unified topological field theory. *Phys. Rev. E* **105**, 024602, DOI: [10.1103/PhysRevE.105.024602](https://doi.org/10.1103/PhysRevE.105.024602) (2022).
48. Kleman, M. & Lavrentovich, O. D. *Soft Matter Physics: An introduction* (Springer, New York, 2003).
49. Zaccane, A. & Scossa-Romano, E. Approximate analytical description of the nonaffine response of amorphous solids. *Phys. Rev. B* **83**, 184205, DOI: [10.1103/PhysRevB.83.184205](https://doi.org/10.1103/PhysRevB.83.184205) (2011).
50. Zaccane, A. *Theory of Disordered Solids* (Springer, Heidelberg, 2023).

51. Wu, Z. W., Chen, Y., Wang, W.-H., Kob, W. & Xu, L. Topology of vibrational modes predicts plastic events in glasses. *Nat. Commun.* **14**, 2955, DOI: [10.1038/s41467-023-38547-w](https://doi.org/10.1038/s41467-023-38547-w) (2023).
52. Desmarchelier, P., Fajardo, S. & Falk, M. L. Topological characterization of rearrangements in amorphous solids (2024). [2401.07109](https://doi.org/10.2401.07109).
53. Dasgupta, R., Hentschel, H. G. E. & Procaccia, I. Microscopic mechanism of shear bands in amorphous solids. *Phys. Rev. Lett.* **109**, 255502, DOI: [10.1103/PhysRevLett.109.255502](https://doi.org/10.1103/PhysRevLett.109.255502) (2012).
54. Hieronymus-Schmidt, V., Rösner, H., Wilde, G. & Zaccone, A. Shear banding in metallic glasses described by alignments of eshelby quadrupoles. *Phys. Rev. B* **95**, 134111, DOI: [10.1103/PhysRevB.95.134111](https://doi.org/10.1103/PhysRevB.95.134111) (2017).
55. Şopu, D. Stz-vortex model: The key to understand stz percolation and shear banding in metallic glasses. *J. Alloy. Compd.* **960**, 170585, DOI: <https://doi.org/10.1016/j.jallcom.2023.170585> (2023).
56. Bera, A., Baggioli, M., Petersen, T. C., Liu, A. C. Y. & Zaccone, A. Soft spots of net negative topological charge directly cause the plasticity of 3d glasses (2024). [2401.15359](https://doi.org/10.2401.15359).
57. Lemaître, A. et al. Anomalous elasticity and plastic screening in amorphous solids. *Phys. Rev. E* **104**, 024904, DOI: [10.1103/PhysRevE.104.024904](https://doi.org/10.1103/PhysRevE.104.024904) (2021).
58. Livne, N. S., Schiller, A. & Moshe, M. Geometric theory of mechanical screening in two-dimensional solids. *Phys. Rev. E* **107**, 055004, DOI: [10.1103/PhysRevE.107.055004](https://doi.org/10.1103/PhysRevE.107.055004) (2023).
59. Nampoothiri, J. N., D'Eon, M., Ramola, K., Chakraborty, B. & Bhattacharjee, S. Tensor electromagnetism and emergent elasticity in jammed solids. *Phys. Rev. E* **106**, 065004, DOI: [10.1103/PhysRevE.106.065004](https://doi.org/10.1103/PhysRevE.106.065004) (2022).
60. Nampoothiri, J. N. et al. Emergent elasticity in amorphous solids. *Phys. Rev. Lett.* **125**, 118002, DOI: [10.1103/PhysRevLett.125.118002](https://doi.org/10.1103/PhysRevLett.125.118002) (2020).
61. Sciortino, F. & Tartaglia, P. Glassy colloidal systems. *Adv. Phys.* **54**, 471–524 (2005).
62. Denisov, D. V. et al. Sharp symmetry-change marks the mechanical failure transition of glasses. *Sci. Reports* **5**, 14359, DOI: [10.1038/srep14359](https://doi.org/10.1038/srep14359) (2015).
63. Klix, C. L., Maret, G. & Keim, P. Discontinuous shear modulus determines the glass transition temperature. *Phys. Rev. X* **5**, 041033, DOI: [10.1103/PhysRevX.5.041033](https://doi.org/10.1103/PhysRevX.5.041033) (2015).
64. Ebert, F., Dillmann, P., Maret, G. & Keim, P. The experimental realization of a two-dimensional colloidal model system. *Rev. Sci. Instruments* **80** (2009).
65. Ebert, F., Keim, P. & Maret, G. Local crystalline order in a 2d colloidal glass former. *The Eur. Phys. J. E* **26**, 161–168, DOI: [10.1140/epje/i2007-10270-8](https://doi.org/10.1140/epje/i2007-10270-8) (2008).
66. Illing, B. et al. Mermin–wagner fluctuations in 2d amorphous solids. *Proc. Natl. Acad. Sci.* **114**, 1856–1861 (2017).
67. Bembenek, S. D. & Laird, B. B. Instantaneous normal modes and the glass transition. *Phys. Rev. Lett.* **74**, 936–939, DOI: [10.1103/PhysRevLett.74.936](https://doi.org/10.1103/PhysRevLett.74.936) (1995).
68. Keyes, T. Instantaneous normal mode approach to liquid state dynamics. *The J. Phys. Chem. A* **101**, 2921–2930, DOI: [10.1021/jp963706h](https://doi.org/10.1021/jp963706h) (1997).
69. Zaccone, A. & Baggioli, M. Universal law for the vibrational density of states of liquids. *Proc. Natl. Acad. Sci.* **118**, e2022303118, DOI: [10.1073/pnas.2022303118](https://doi.org/10.1073/pnas.2022303118) (2021).
70. Stamper, C., Cortie, D., Yue, Z., Wang, X. & Yu, D. Experimental confirmation of the universal law for the vibrational density of states of liquids. *The J. Phys. Chem. Lett.* **13**, 3105–3111, DOI: [10.1021/acs.jpcclett.2c00297](https://doi.org/10.1021/acs.jpcclett.2c00297) (2022). PMID: 35362320.
71. Ramos, M. A. *Low-temperature Thermal and Vibrational Properties of Disordered Solids: A Half-century of Universal "anomalies" of* (World Scientific, 2022).
72. Chen, K. et al. Low-frequency vibrations of soft colloidal glasses. *Phys. Rev. Lett.* **105**, 025501, DOI: [10.1103/PhysRevLett.105.025501](https://doi.org/10.1103/PhysRevLett.105.025501) (2010).
73. Guo, X. et al. Near-field localization of the boson peak on tantalum films for superconducting quantum devices. *The J. Phys. Chem. Lett.* **14**, 4892–4900, DOI: [10.1021/acs.jpcclett.3c00850](https://doi.org/10.1021/acs.jpcclett.3c00850) (2023). PMID: 37199508.
74. Tømterud, M. et al. Observation of the boson peak in a two-dimensional material. *Nat. Phys.* **19**, 1910–1915, DOI: [10.1038/s41567-023-02177-2](https://doi.org/10.1038/s41567-023-02177-2) (2023).

75. Palyulin, V. V. et al. Parameter-free predictions of the viscoelastic response of glassy polymers from non-affine lattice dynamics. *Soft Matter* **14**, 8475–8482, DOI: [10.1039/C8SM01468J](https://doi.org/10.1039/C8SM01468J) (2018).
76. Zhang, W., Douglas, J. F. & Starr, F. W. What does the instantaneous normal mode spectrum tell us about dynamical heterogeneity in glass-forming fluids? *The J. Chem. Phys.* **151**, 184904, DOI: [10.1063/1.5127821](https://doi.org/10.1063/1.5127821) (2019). <https://doi.org/10.1063/1.5127821>.
77. Mizuno, H. & Ikeda, A. Computational simulations of the vibrational properties of glasses. In *Low-Temperature Thermal and Vibrational Properties of Disordered Solids: A Half-Century of Universal “Anomalies” of Glasses*, 375–433 (World Scientific, 2023).
78. Smessaert, A. & Rottler, J. Structural relaxation in glassy polymers predicted by soft modes: a quantitative analysis. *Soft Matter* **10**, 8533–8541, DOI: [10.1039/C4SM01438C](https://doi.org/10.1039/C4SM01438C) (2014).
79. Plimpton, S. Fast parallel algorithms for short-range molecular dynamics. *J. Comp. Phys* **117**, 1–19 (1995). See also: <http://lammps.sandia.gov>.

# Supplementary Information

In this Supplementary Information (SI) we provide additional details about the experimental conditions and setup, a brief description of the structure and dynamics of the system, and some simulation results to complement the experimental observation.

## Additional information related to the experiment

Experimental information has been described in detail in [64], but we briefly outline here the crucial steps. Our system consists of a binary colloidal mixture having paramagnetic properties, suspended at a flat air-water interface due to gravity. The tilt and interface position is well controlled throughout the simulation to realize a perfect two-dimensional system. In the presence of an external magnetic field, for the typical inter-particle separation at room temperature, the dominating interaction between particles is dipole-dipole interaction.

**Superparamagnetic colloidal particles:** The colloidal particles are polystyrene beads doped with magnetite ( $\text{Fe}_2\text{O}_3$ ) and sealed with a thin layer of epoxy. In the absence of an external magnetic field, net magnetization in each colloidal particle is zero. There are two types of particles (diameters:  $d_A = 4.5 \pm 0.05 \mu\text{m}$ ,  $d_B = 2.8 \mu\text{m}$ ; mass density:  $\rho_A = 1.5 \text{ g/cm}^3$ ,  $\rho_B = 1.3 \text{ g/cm}^3$  and magnetic susceptibility per particle:  $\chi_A = 6.22 \times 10^{-11} \text{ Am}^2/\text{T}$ ,  $\chi_B = 6.6 \times 10^{-12} \text{ Am}^2/\text{T}$ ). Particles observed under transmission electron microscopy show that the magnetite is uniformly distributed over each particle volume and bigger particles are quite monodisperse. Smaller particles may have small polydispersity.

Suspensions of bigger and smaller particles are prepared separately and after treating properly to make sure that the suspension is uniform and there is no particle aggregation, they are mixed properly to get the mixture with the desired composition  $\xi = N_A/(N_A + N_B)$ ;  $N_A$  and  $N_B$  are the numbers of bigger and smaller species respectively. For the present colloidal system, we have an equal number of bigger and smaller species, i.e.,  $\xi \approx 0.5$ .

**Experimental setup: Formation of air-water interface and its control:** A cylindrical hole of diameter 6 mm and depth 1 mm is created in a glass plate. A water droplet hangs inside this cylindrical geometry due to surface tension. The bottom air-water interface hosts the suspension of binary colloidal mixture after sedimentation due to gravity, while the top of the interface is properly sealed. A computer-controlled microsyringe attached horizontally controls the volume of the pending drop to ensure a flat interface. A schematic diagram of this setup is shown in Fig. 1 of the main text. The colloidal particles can freely diffuse over the interface, in contrast to other experimental setups where such a system is realized over a substrate, it is difficult to avoid the pinning of a few particles. The curvature and inclination of the interface have been adjusted over months to achieve a gradient-free density profile. There are copper coils that generate an almost uniform magnetic field, compensating the earth's magnetic field, in the plane of the sample (deviation is less than 0.5% in the field of interest).

Video microscopy is employed to visualize the particles from the below side of the sample and an 8-bit charge-coupled device camera records the gray scale images of particles which are analyzed by a computer. There are approximately  $10^5$  particles in the sample but the camera has the field of view of  $\approx 1 \text{ mm}^2$  ( $1158 \times 865 \mu\text{m}^2$ ) which can capture about 2300 particles. In this setup, the particle trajectories can be recorded for several days with the spatial resolution of  $\approx 50 \text{ nm}$  and a time resolution of  $\approx 1 \text{ s}$ .

For the analysis presented in the main text, we have utilized 1000 configurations sampled over a period of 2772 seconds. Throughout the experiments, room temperature is maintained.

## Structure and dynamics of the colloidal system

As discussed in the main article,  $\Gamma$ , which is the ratio of magnetic dipole-dipole interaction energy to thermal energy ( $k_B T$ ):

$$\Gamma = \frac{\mu_0 (\pi n)^{3/2}}{4\pi k_B T} [\xi \chi_B + (1 - \xi) \chi_A]^2. \quad (9)$$

Here,  $n$  is the area density computed via Voronoi tessellation.  $\Gamma$  for the sample used in this study is 423. At this value of  $\Gamma$ , the structure and dynamics of the system are of a typical glass. We present below the pair-correlation function and mean-squared displacement (MSD) of the sample.

Partial pair-correlations in Fig. 6 indicate that the mixture is homogeneous and the structure is disordered. MSD plotted in Fig. 7 has an extended plateau, this means that the dynamics of the system is largely arrested. These features establish the typical glassy behavior of the samples used in this study.

## Charge density and Softness map

In order to calculate the topological charge density, we have divided the entire experimental box into square cells of size  $a_s = 20.78 \mu\text{m}$  and then count the number of topological defects  $np$  and  $nm$  with winding numbers  $+1$  and  $-1$ , respectively, for

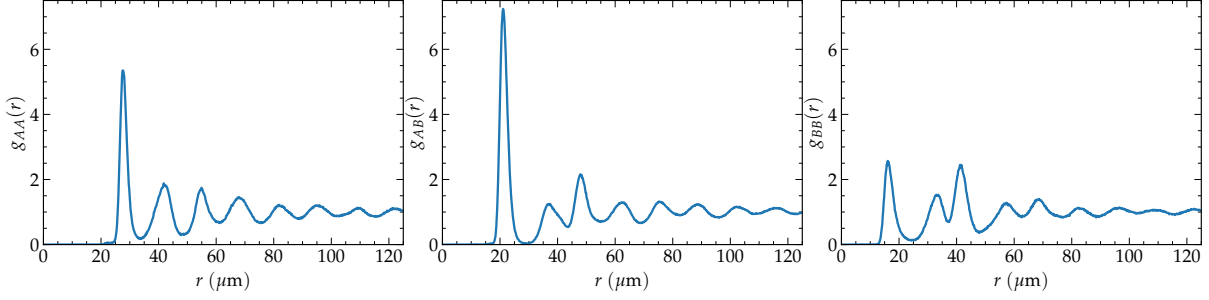


**Figure 6.** Partial pair correlation functions  $g_{AA}(r)$ ,  $g_{AB}(r)$  and  $g_{BB}(r)$  calculated for the samples used in the study.

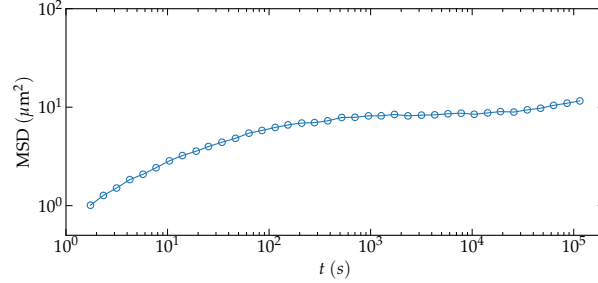


**Figure 7.** Mean squared displacement (MSD) as a function of time.

each  $\omega \in (0, 50)$ . Then the average charge density inside each square cell is defined as

$$\bar{c} = \frac{\sum_i (np - nm) / \omega_i}{\sum_i 1 / \omega_i}. \quad (10)$$

Here we have used the weighted factor  $1/\omega$  due to the linear dependence of the total number of defects at lower frequencies.

## Additional simulation results

We have also performed a set of simulations of a two dimensional Lennard-Jones glass as that studied by Wu et al. in [51]. We have extended their analysis of vibrational spectra and topological features to finite temperature systems, to better compare with our experimental setup. We aim to understand whether the low-frequency behavior of  $N_d$ , *i.e.*, the total number of topological defects changes for finite temperature glasses. We perform additional simulations of thermal glass with the athermal one using LAMMPS [79]. Thermalized glassy configurations are prepared by cooling the high-temperature glass at  $T_i = 5.0$  to the target temperatures  $T = 0.1, 0.2, 0.4$  over  $10^7$  time step ( $\delta t = 0.001$ ) and then annealed for further  $10^6$  number of time steps. For the preparation of athermal configurations, we have followed the same protocol as discussed in [51]; energy of  $T = 0.1$  glassy configuration is minimized using conjugate gradient algorithm.

We calculate the vibrational density of states using the instantaneous configurations at different temperatures and characterize the topological defects in the eigenspace. The fraction of unstable modes grows with temperature, in contrast to the athermal case where such modes are absent. Our focus is on the small omega behavior of  $N_d$  with the temperature change. In Fig. 8 we observe that, unlike the athermal case where  $N_d \sim \omega^\alpha$  with  $\alpha = 2$ , the scaling of the number of defects with frequency becomes linear at finite temperature. Our experimental colloidal system is a finite temperature glass, as the presence of imaginary modes in the vibrational spectrum confirms. Consistent with this simulation analysis, the scaling of the number of defects in the experimental system shows an exponent  $\alpha$  close to 1.

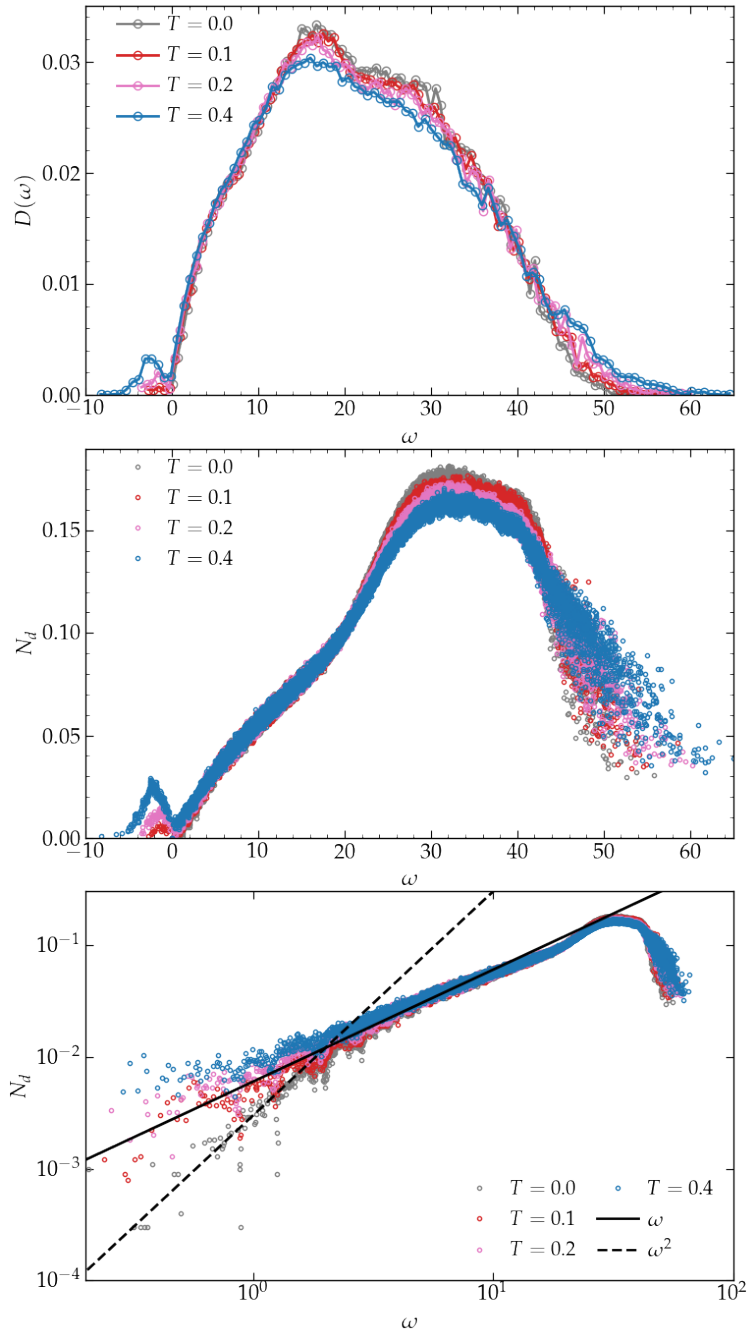


**Figure 8.** Vibrational density of states  $D(\omega)$  and number of topological defects  $N_d$  as a function of frequency  $\omega$  at different temperatures in a two dimensional Lennard-Jones glass.